








Control over epitaxy and the role of the InAs/Al interface in hybrid two-dimensional electron gas systems

Erik Cheah ^{1,2,*}, Daniel Z. Haxell,³ Rüdiger Schott ^{1,2}, Peng Zeng ⁴, Ekaterina Paysen ⁵, Sofieke C. ten Kate,³ Marco Coraiola,³ Max Landstetter ¹, Ali B. Zadeh ⁴, Achim Trampert,⁵ Marilyne Sousa,³ Heike Riel,³ Fabrizio Nichele,³ Werner Wegscheider,^{1,2} and Filip Krizek ^{1,3,6}

¹*Solid State Physics Laboratory, ETH Zurich, 8093 Zurich, Switzerland*

²*Quantum Center, ETH Zurich, 8093 Zurich, Switzerland*

³*IBM Research Europe - Zurich, 8803 Rüschlikon, Switzerland*

⁴*ScopeM, ETH Zurich, 8093 Zurich, Switzerland*

⁵*Paul-Drude-Institut für Festkörperelektronik, Leibniz-Institut im Forschungsverbund Berlin e. V., 10117 Berlin, Germany*

⁶*Institute of Physics, Czech Academy of Sciences, 162 00 Prague, Czech Republic*



(Received 18 January 2023; accepted 2 June 2023; published 26 July 2023)

In situ synthesized semiconductor/superconductor hybrid structures became an important material platform in condensed matter physics. Their development enabled a plethora of novel quantum transport experiments with focus on Andreev and Majorana physics. The combination of InAs and Al has become the workhorse material and has been successfully implemented in the form of one-dimensional structures and two-dimensional electron gases. In contrast to the well-developed semiconductor parts of the hybrid materials, the direct effect of the crystal nanotexture of Al films on the electron transport still remains unclear. This is mainly due to the complex epitaxial relation between Al and the semiconductor. Here, we present characterization of Al thin films grown on shallow InAs two-dimensional electron gas systems by molecular beam epitaxy. Using a growth approach based on an intentional roughening of the epitaxial interface, we demonstrate growth of grain-boundary-free Al. We show that the implemented roughening does not negatively impact either the electron mobility of the two-dimensional electron gas or the basic superconducting properties of the proximitized system. This is an important step in understanding the role of properties of the InAs/Al interface in hybrid devices. Ultimately, our results provide a growth approach to achieve a high-degree of epitaxy in lattice-mismatched materials.

DOI: [10.1103/PhysRevMaterials.7.073403](https://doi.org/10.1103/PhysRevMaterials.7.073403)

I. INTRODUCTION

Material systems that combine semiconductors (SEs) and superconductors (SCs) have recently prompted novel research directions in condensed matter physics. The main motivation to study these systems are different approaches to quantum computing, e.g., Andreev [1] and transmon qubits [2,3] or topological systems hosting Majorana bound states [4].

The combination of InAs and *in situ* deposited Al has become an established material platform, either in the form of proximitized quasi-one-dimensional hybrid nanowires or shallow (near-surface) two-dimensional electron gas (2DEG) systems [5,6]. The choice of InAs as the semiconducting part is due to its relatively large spin-orbit coupling and advantageous band alignment at the SE/SC interface [7]. Furthermore, it exhibits good etching selectivity and chemical stability in device fabrication processes. The choice of Al

is motivated by the possibility to achieve a high degree of epitaxial order on InAs [5], as well as by the fact that Al and InAs are mutually compatible with *in situ* deposition in typical III-V molecular beam epitaxy (MBE) systems, which often contain both the In and Al sources.

An important aspect of the hybrid material is that no sub-gap states are present in the hard superconducting gap. This was first shown for InAs nanowires with epitaxial Al thin films [8]. The hard superconducting gap was attributed to the formation of a fully epitaxial InAs/Al interface, forming when the Al film was deposited *in situ* in the same MBE system where the InAs nanowires were grown [5]. Such nanowire-based systems exhibit great promise as a platform for investigating transport phenomena [9–11]. However, the lack of reliable schemes for scaling up to large device arrays limits their perspective for industrial applications.

The complementary systems based on shallow InAs 2DEGs coupled to superconductivity via proximity to an Al thin film show more promise for large-scale applications [6,12], due to their compatibility with top-down fabrication techniques [13]. Yet, a different issue arises in comparison to the InAs NW based system, since the strain relaxation of Al is reduced from three to two spatial degrees of freedom. This promotes the formation of Al grains of different orientations within the same *in situ* deposited Al film and disturbs the

*echeah@phys.ethz.ch

Published by the American Physical Society under the terms of the [Creative Commons Attribution 4.0 International](https://creativecommons.org/licenses/by/4.0/) license. Further distribution of this work must maintain attribution to the author(s) and the published article's title, journal citation, and DOI.

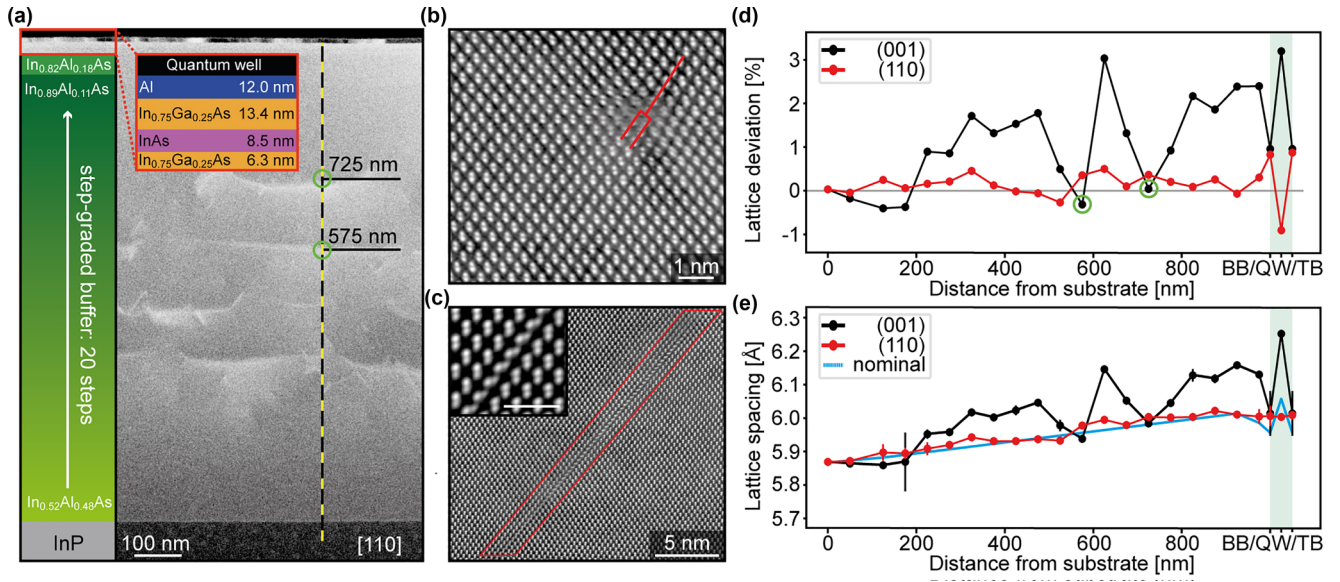


FIG. 1. (a) ADF-STEM image of the shallow InAs 2DEG structure. A schematic of the structural design is shown in the left panel, with the zoom-in inset showing the detailed structure of the quantum well region. The yellow dashed line highlights locations of the images used for the lattice constant evaluation. The 575 nm and 725 nm markers along the line highlight regions where a change in the ADF contrast indicates strain relaxation. (b) HAADF-STEM image of a single misfit dislocation. (c) ADF-STEM image of an extended twin defect, with a higher magnification image in the inset (scale bar is 1 nm). (d) The deviation of the measured lattice spacing as a function of the distance from the substrate (extracted from HAADF-STEM images taken in the center of each grown layer) from the bulk lattice constant for the individual layers. The lattice spacing is evaluated from the spacings of both the (001) and (110) planes. BB stands for bottom barrier, QW for quantum well, and TB for top barrier, which are plotted in the green shaded area. The local minima (green circles) correspond to locations of local strain relaxation highlighted in (a). (e) Same dependency, but for the lattice spacing of each individual layer in the structure. The blue line shows the bulk lattice constant of each layer.

homogeneity of the epitaxial interface [14–16]. There are indications that related formation of grain boundaries can have a significant effect on the properties of superconducting thin films. As an example, the critical temperature and critical magnetic field can dramatically change in granular Al [17,18]. A different study has shown that the presence of grain boundaries can promote local oxidation of the Al and therefore affect its superconducting properties [19].

Despite local disturbances of the epitaxial interface a hard superconducting gap was also reported for Al *in situ* deposited on InAs 2DEG structures [20]. On the other hand, the effect of disorder on other features of electron transport in the hybrid system remains vastly unexplored, despite that recent studies have suggested that local disorder in superconducting films could play a key role in the functionality of superconducting qubits [21,22] and proximitized SE/SC devices [23–25]. Therefore, experimental understanding of the effect of different structural features of the SE/SC interface on electron transport is of great importance. Especially decoding the exact experimental limitations that have to be imposed on the material quality would be of great benefit in designing new hybrid materials and exploring new material combinations [26–32].

In this work, we introduce a growth method that can improve the degree of epitaxy in lattice mismatched heterostructures by implementing intentional roughening of the epitaxial interface. This is likely applicable for different materials and partially contradicts the typical efforts to improve quality of heterostructures by hunting for atomically flat pristine interfaces. We demonstrate the applicability of

the method by achieving control over crystallinity of epitaxial Al films *in situ* deposited on optimized shallow InAs 2DEGs. First, we analyze the strain evolution in the structure and identify the two dominant grain orientations responsible for the presence of two distinct epitaxial relations at the SE/SC interface. Furthermore, we use the newly established controlled roughening of the SE surface to improve the Al quality, i.e., to grow grain-boundary-free Al films over scales of at least 5 μm . Finally, we characterize the material by fabricating and measuring hybrid Josephson junctions (JJs) and in contrast to general expectations find that the roughening does not negatively impact its transport properties.

II. GROWTH OF THE SEMICONDUCTOR

The superconducting Al thin films were deposited on shallow (near-surface) InAs-based 2DEG semiconductor platform [6] grown on semi-insulating Fe-doped (001) InP substrates by MBE. The structure of the semiconductor consists of three main elements: (i) Step-graded $\text{In}_x\text{Al}_{1-x}\text{As}$ buffer used to compensate for the lattice mismatch between the substrate and the InAs QW. (ii) InAs based QW confined by $\text{In}_{0.75}\text{Ga}_{0.25}\text{As}$ barriers. (iii) GaAs cap, which is used to prevent diffusion of In to the subsequently deposited Al thin film and/or roughen the SE surface in a controlled manner. The full structure is illustrated and shown in the annular dark field (ADF) scanning transmission electron microscope (STEM) image in Fig. 1(a).

In more detail, the step-graded metamorphic $\text{In}_x\text{Al}_{1-x}\text{As}$ buffer layer consisted of 20×50 nm steps with x increasing

from 0.52–0.89 and a step-back layer to a virtual substrate with $x = 0.82$. The QW region consisted of a 8.5 nm thick InAs layer embedded between $\text{In}_{0.75}\text{Ga}_{0.25}\text{As}$ barriers. For the purpose of this study, we fixed the bottom barrier to a thickness of 6.3 nm, the top barrier thickness to 13.4 nm and the GaAs cap to two monolayers (MLs). Samples with this structure will be further referred to as standard samples. The standard samples showed a good ratio of as-grown SE mobility and the strength of the induced proximity effect [33–36]. Electron mobility of $\sim 50000 \text{ cm}^2/(\text{V} \cdot \text{s})$ at electron densities $\sim 4 \times 10^{11} \text{ cm}^{-2}$ was measured in the van der Pauw configuration at 4.2 K ($5 \times 5 \text{ mm}^2$ samples). For these high-mobility samples, we also observed a surface with strongly anisotropic crosshatching. A detailed description of the SE growth parameters and their influence on the surface morphology is given in Supplemental Material [36].

To further study the properties of our InAs 2DEGs, we grew a series of samples with a top-barrier thickness variation. As will be shown below, increasing the barrier thickness significantly enhances the electron mobility, but has an opposite effect on the strength of the proximity induced superconductivity. Interestingly, we managed to proximitize devices with top barrier thickness above the expected theoretical limit given in Ref. [6]. This should be thoroughly investigated in future works, as the proximity effect in hybrid materials is expected to be affected by the interplay of strain, material composition of the barrier, QW dimensions, quality of the Al film and the epitaxial interface.

Strain is one of the important aspects of the SE structure and can strongly affect its transport properties, but also the epitaxial relation to the Al film. Strain fields related to defect formation and lattice relaxation in the $\text{In}_x\text{Al}_{1-x}\text{As}$ metamorphic buffer are clearly visible in the ADF STEM image in Fig. 1(a). Importantly, they do not extend into the QW region, which remains defect free. The most abundant defects, which dominate the relaxation and generate the strain fields, are shown in high angle annular dark field (HAADF) STEM images in Figs. 1(b) and 1(c). The first type of an abundant defect, shown in Fig. 1(b), are isolated misfit dislocations. The second type are single twin planes extending over tens of nanometers, shown in Fig. 1(c). Both defect types are randomly distributed throughout the strain relaxation region.

To further understand the strain distribution within the structure, we extracted the lateral and vertical lattice spacings [along $(1\bar{1}0)$ and (001) directions] from STEM images taken in the center of each layer of the structure, as illustrated in Fig. 1(a) and in the Supplemental Material [36]. A percentual deviation from the bulk lattice constant is plotted as a function of distance from the substrate in Fig. 1(d). As expected, the (110) deviation evolves in a stable manner throughout the whole structure, while the (001) deviation shows strong local variations. Specifically, there are two local minima that overlap with the most strained regions visible in Fig. 1(a). The lateral (110) lattice spacing remains almost constant in the QW region, which is expected for growth on a relaxed virtual substrate and is shown in Fig. 1(d). The average spacing and deviation is $6.00 \pm 0.02 \text{ \AA}$ for the bottom barrier, QW and top barrier, which yields 0.9% compressive strain. We observed a similar relaxation behavior in multiple

samples. The negligible variation of the lattice constant close to the surface of the semiconductor is important for consistent investigation of the epitaxial relation to the superconducting Al film, which will be further discussed below.

III. Al THIN FILMS

Prior to the *in situ* Al deposition on the above-described semiconductor platform, the samples were moved to an ultrahigh vacuum buffer chamber (1×10^{-11} mbar) directly after growth of the shallow InAs 2DEG. Subsequently, they were retransferred back to the growth chamber when its pressure reached 1×10^{-10} mbar, i.e., once the As background dropped after closing the As valve. The samples were then passively cooled down for 12 h to reach approximately -30°C . No active cooling was involved and therefore the cooling power is only related to the MBE system being set to idle state and the sample holder being rotated towards the LN_2 cooled cryoshrouds. After the cool down, the Al films (12 nm thick in samples used in the presented transport experiments) were deposited at a rate of 1 \AA/s at a pressure of $3\text{--}5 \times 10^{-11}$ mbar in the growth chamber. We note that the sample surface must remain cold during the deposition. Therefore, the used growth rate (controlled by the cell temperature) needs to be optimized for each specific MBE system geometry, as it determines heat delivered to the surface of the sample during growth.

After the Al deposition, the wafer was moved to the load lock chamber (below 5×10^{-10} mbar). In order to prevent thermal dewetting of the Al film by warming to ambient temperature in the ultrahigh vacuum, the samples were transferred as fast as possible to the load lock. To oxidize the Al surface in a controlled way, the load lock was vented with an Ar/O_2 (90/10 %) mixture over the course of 15 min while bringing the wafer to 25°C . In contrast to this procedure, control samples that were unloaded using pure Ar, meaning that the Al surface was subsequently oxidized by exposure to ambient atmosphere, exhibited larger surface roughness as shown in the Supplemental Material [36].

In our standard samples we mainly observe the presence of two distinctly oriented grains of Al. The first type is shown in Fig. 2. In this case, the Al with (111) out-of-plane orientation adapts either (112) in Fig. 2(a) or (110) in Fig. 2(b) lateral matching to the (110) planes of the semiconductor [here labeled as Al:A(112) and Al:A(110)]. Therefore in STEM, it is possible to observe two distinct projections and epitaxial relations of the Al:A crystal, depending on its alignment to the substrate. For the Al:A(112) orientation shown in Fig. 2(a), we observe a clean, fully epitaxial interface, with apparent (and ordered) intermixing within the first matching monolayers. For the Al:A(110) orientation shown in Fig. 2(b), we observe 5×3 matching, i.e., there are two misfit dislocations at the interface per three planes in the substrate.

The second grain type is shown in Fig. 3, where the Al adapts (011) out-of-plane orientation and lateral matching as either (001) in Fig. 3(a) or (110) in Fig. 3(b) to the (110) planes of the semiconductor [here labeled as Al:B(001) and Al:B(110)]. For this grain, we observe formation of misfit dislocations for both alignments to the (110) planes of the semiconductor. For the Al:B(001) matching, the film relaxes by the formation of periodic arrays of misfit dislocations with

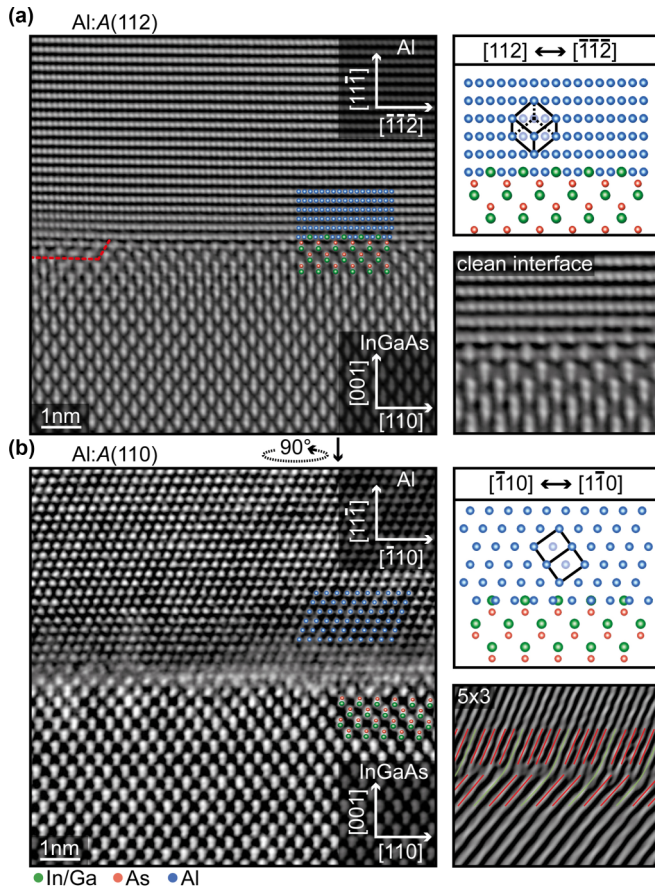


FIG. 2. (a) HAADF-STEM image of the interface between an Al:A(112) grain and the semiconductor, showing Al(112) to SE(110) lateral matching. Both the image and the model (top right panel) show an undisturbed epitaxial matching. The red line highlights coherent matching over a step on the SE surface. (b) HAADF-STEM image of a grain of the same orientation (Al:A), but rotated by 90° around the [111] axis, i.e., showing Al(110) to SE(110) matching (Al:A(110)). The Bragg-filtered image (bottom right panel) shows that the lattice mismatch along this direction is relaxed by networks of misfit dislocations with Al \times SE 5×3 periodicity. Local contrast was normalized in all the STEM images.

larger spacing. In contrast, there is a single misfit dislocation per two planes in the substrate, i.e., a 3×2 match for the Al:B(110) orientation. We observed that both grain types were equally present in the samples and often adapted small tilts [e.g., the slight tilt visible in Fig. 3(a)]. A larger scale ADF-STEM overview of such a sample is shown in the top panel of Fig. 4(a). The changing ADF contrast indicates a high density of grains with different orientation. The contrast can originate from the two different types of grains, mutual tilt of grains with the same orientation and/or from the two possible projections (i.e., 90° grain rotation). An example of a boundary between the two different grain types is shown in Fig. 4(b). The smoothness of the SE surface in the HAADF STEM image indicates that the presence of the boundary is not associated with neither a surface step nor a crystallographic defect in the semiconductor.

These partially polycrystalline Al films performed consistently with previous reports in literature in our transport

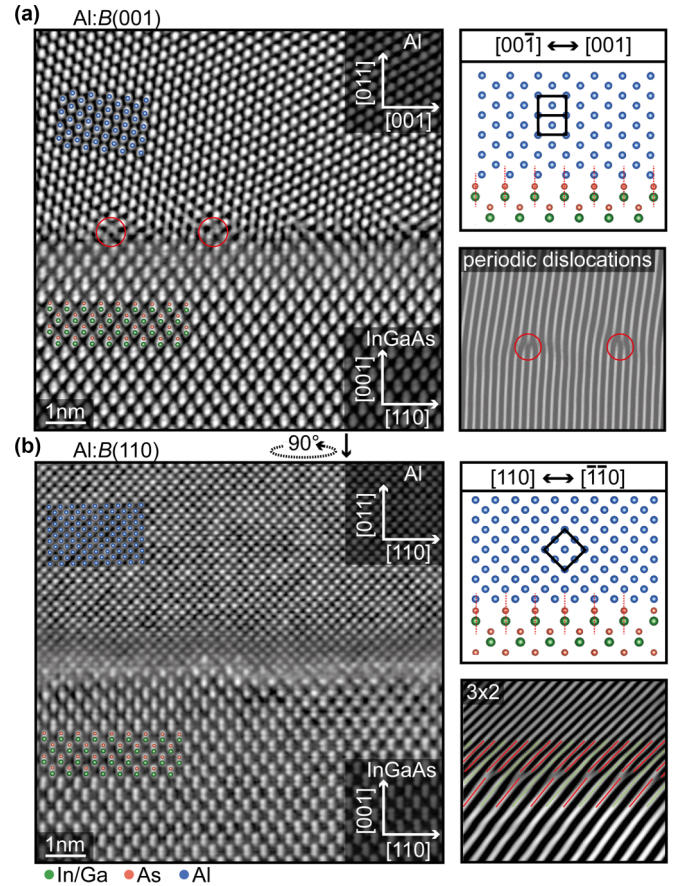


FIG. 3. (a) HAADF-STEM image of the interface between an Al:B(001) grain and the semiconductor, showing Al(001) to SE(110) lateral matching. The Bragg-filtered image (bottom right panel) shows that the strain along this direction is relaxed by the typical formation of misfit dislocations (highlighted by red circles). (b) HAADF-STEM image of a grain of the same orientation (Al:B), but rotated by 90° around the [011] axis, i.e., showing Al(110) to SE(110) matching (Al:B(110)). Both the image and the model (top right panel) show significant mismatch. The Bragg-filtered image (bottom right) shows that the lattice mismatch along this direction is relaxed by networks of misfit dislocations with Al \times SE 3×2 periodicity. Local contrast was normalized in both STEM images.

experiments, which rely on the combined SE/SC system [33–36]. On the other hand, consistent results were achieved only when processing temperatures did not exceed 175°C . This is due to degradation of both the Al film and the SE/Al interface, which was investigated by *in situ* annealing of a lamella prepared from the standard material in a scanning transmission electron microscope. While ramping the temperature up to 225°C , we observed degradation of individual grains into amorphous Al, diffusion grain boundaries and also intermixing of Al at the interface and even local recrystallization into a zinc-blende structure, as reported in the Supplemental Material [36]. Reaching such high temperatures during device fabrication had a negative impact on the transport properties of the material and the fabricated devices could not be further utilized in our experiments. The observed degradation is also expected to happen in the smallest features of our devices, since their dimensions are

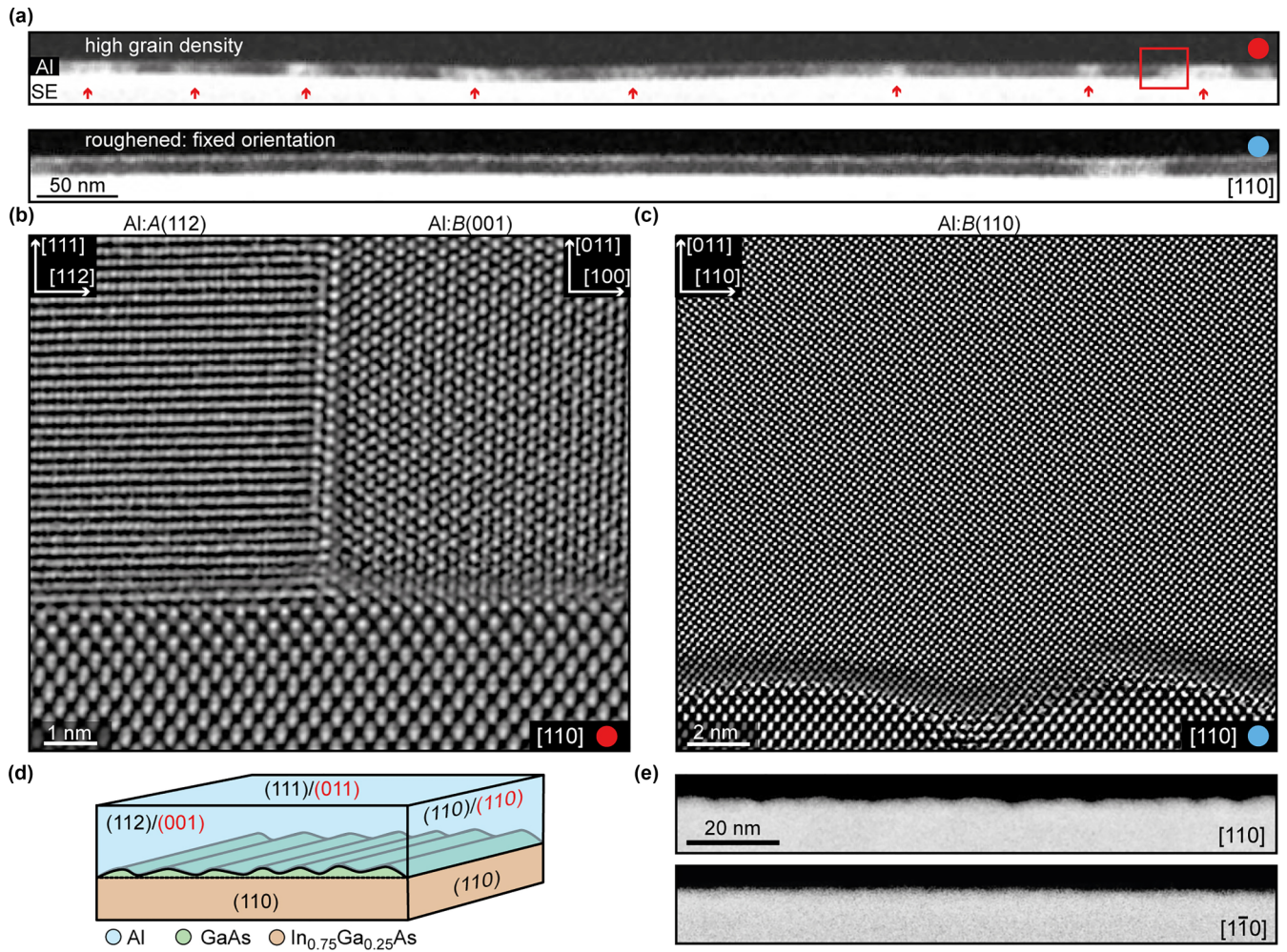


FIG. 4. (a) ADF-STEM images of high grain density (top) and a single orientation (bottom) Al thin films. The red arrows highlight regions with strong changes in contrast. (b) A higher magnification and contrast normalized HAADF image showing structure of one of the possible grain boundaries, highlighted by red arrows in (a). (c) Contrast normalized HAADF-STEM image of an Al film deposited on a roughened surface. (d) Schematic of the possible orientations of different Al films on a heavily anisotropically roughened surface. (e) HAADF-STEM images of two perpendicular projections ([110] and $[1\bar{1}0]$) of the top interface of the semiconductor, demonstrating the anisotropy and scale of the intentional roughening. Local contrast normalization was performed for images in (b) and (a).

often comparable to the lamella ($5\ \mu\text{m}$ in length and below $50\ \text{nm}$ thick). Importantly, the observed recrystallization was selective to the specific grain type and some of the investigated grains remained crystalline and their interface to the SE was stable even at $225\ ^\circ\text{C}$. This difference in thermal energy necessary to dissolve the interface for specific grain types needs to be considered during development of fabrication processes and is one of the motivations to develop growth of single crystalline Al films on InAs 2DEGs.

IV. EFFECT OF ROUGHENING ON CRYSTALLOGRAPHY

The Al film is locked into a single orientation using intentional roughening of the semiconductor surface by deposition of more than the standard 2 MLs GaAs on the In_{0.75}Ga_{0.25}As top barrier. This is shown for a sample capped with 5 MLs of GaAs prior the Al deposition in the bottom panel of Fig. 4(a). In such films, we did not detect the presence of any grain boundaries, i.e., grains with different orientations over a range of $5\ \mu\text{m}$, the typical size of our investigated lamellae.

We found that nanoscale surface roughening of the SE induced by GaAs deposition is anisotropic along the [110] and $[1\bar{1}0]$ directions, as shown in the STEM images in Fig. 4(e) and as investigated by STEM tomography [37] in the Supplemental Material [36]. This is likely related to highly anisotropic diffusion of Ga atoms during deposition at elevated temperatures [38] and a large mismatch between the In_{0.75}Ga_{0.25}As top barrier and GaAs cap [39].

The nanoscale roughening of the SE surface seems to affect the orientation of the Al in two ways, summarized in Fig. 4(c). First, it leads to a selectivity of the out-of-plane grain orientation and reduced formation of grain boundaries. Similarly, growth on roughened or nanopatterned substrates, i.e., nanoheteroepitaxy, was previously used to reduce formation of threading dislocations and residual strain in heterostructures with highly mismatched materials [40,41]. Second, the modulation of the SE surface locks the in-plane orientation into either the Al:A or Al:B grains, so that the {110} planes of the Al align with the $(1\bar{1}0)$ planes of the SE. Both effects are likely related to the enhanced 3D character of the roughened

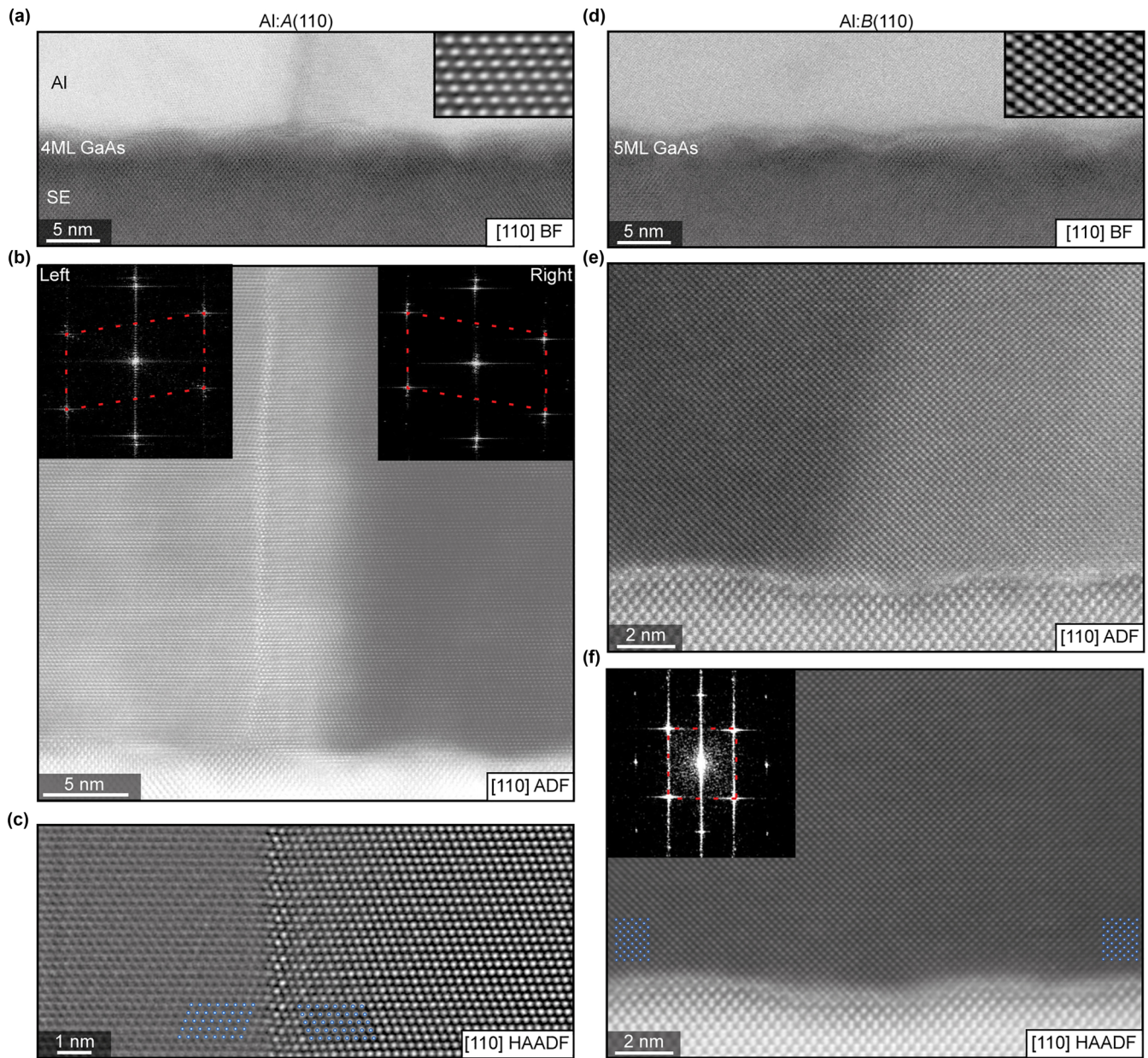


FIG. 5. (a) BF-STEM image of Al films deposited on a surface capped with 4 MLs of GaAs showing a change of contrast in the center. The HAADF image in the inset shows the orientation of the Al film. (b) ADF-STEM image, showing the origin of the contrast in (a). The fast Fourier transform in the inset shows that the Al crystal is mirrored over the boundary. (c) Contrast normalized HAADF image of the crystal around the boundary. (d) BF-STEM image of Al films deposited on a surface capped with 5 MLs of GaAs. The HAADF-STEM image in the inset shows the orientation of the Al film. (e) ADF-STEM image, showing an abrupt change in contrast in the same film as in the bottom panel of Fig. 4(a). (f) HAADF-STEM image of the same area. The fast Fourier transform does not show a detectable change in the crystal structure.

surface, which gives the Al layer an additional degree of freedom for strain relaxation.

We observed this behavior in samples where the $\text{In}_{0.75}\text{Ga}_{0.25}\text{As}$ top barrier was capped with more than 3 MLs of GaAs. An example is shown in Fig. 5, where the Al layer is locked in Fig. 5(a) as Al:A(110) after capping with 4 MLs of GaAs and Fig. 5(b) as Al:B(110) after capping with 5 MLs of GaAs. For the sample capped with 4 MLs GaAs in Fig. 5(a), we observed that the Al only adapted the Al:A(110) orientation. Surprisingly, we observed regions with abruptly changing bright field (BF) and ADF contrast in the STEM images. Yet, this contrast was not related to a major change

in the crystal orientation, but to mirroring with respect to the Al(111) planes, as shown in Fig. 5(b). This is apparent from the mirroring of the fast Fourier transform spectra and the atomic arrangement in the HAADF-STEM zoom in Fig. 5(c). This implies that even when the whole Al film is locked as Al:A{110}, the Al:A($\bar{1}10$) and Al:A($1\bar{1}0$) are not degenerate in this grain orientation. Hence, the Al film in this crystal orientation is naturally prone to twinning and the related formation of incoherent grain boundaries.

This is different for a sample capped with 5 MLs of GaAs, shown in Fig. 5(d), where the crystal orientation was locked into Al:B(100). Similarly to the previous case, the lateral

matching to the substrate was fixed as Al(110) to SE(110) for the whole layer. In this case, we detected only subtle differences in ADF and BF contrast, as shown in Fig. 5(e). Such a detail in the acquired image of the Al layer corresponds to the region of the film with a change in contrast shown in the bottom panel of Fig. 4(a). These changes of contrast were sparse in the films and are likely related to subtle tilts of the crystal, as no apparent crystallographic change was seen in neither the HAADF-STEM image nor the fast Fourier transform in Fig. 5(f). Compared to Al:A, the symmetry of Al:B type grain with respect to the {110} in-plane direction results in the formation of a fully single crystalline film. The subtle observed tilts might be related to relaxation of the strain induced by natural bending of the lamella for samples incorporating metamorphic buffer layers. We note that the differences in the capping layer thickness used in this study are at the experimental limits even with the utilized MBE technique. A consistent study of the capping layer thickness is needed in future works to gain full control over the Al grain growth selectivity.

In addition, we observed that the grain distribution in the films was affected by various additional factors, such as lamella preparation, strain, oxidation, etc., which complicated the capability to perform consistent studies. Also, the Al film degraded and new grains appeared if the lamella was stored in ambient conditions for more than one month, indicating room-temperature recrystallization in the films, as shown in the Supplemental Material [36].

V. EFFECT OF ROUGHENING ON TRANSPORT PROPERTIES

Even though the reduction of grain boundaries by surface roughening offers many benefits in terms of the crystal structure of the Al films, as discussed above, it is crucial to maintain the transport properties of the 2DEG. In Fig. 6(a), we compare magnetotransport measurements of the roughened and standard materials. The measurements were performed in a van der Pauw configuration at 4 K on 5×5 mm as-grown samples after the Al film was removed by wet etching. For the standard nonroughened surface we measured an electron mobility of $53000 \text{ cm}^2/(\text{V} \cdot \text{s})$ at an electron density of $4.0 \times 10^{11} \text{ cm}^{-2}$. For the sample with the same structure but intentionally roughened surface (5 MLs of GaAs) we measured $51000 \text{ cm}^2/(\text{V} \cdot \text{s})$ at an electron density of $3.5 \times 10^{11} \text{ cm}^{-2}$. The Drude mobility and charge carrier density do not significantly change for the roughened sample. We consider this difference to be negligible, since the properties and chemistry of the surface were reported to have a strong effect on the transport in shallow InAs 2DEGs [42,43]. We observed clear quantum Hall and Shubnikov-de Haas transport features at higher magnetic fields in both samples. The variation in quantum Hall behavior at higher magnetic fields can be related to the difference in electron density and sample geometry, for example. In practical applications of the hybrid material, the rather low critical magnetic field of the superconducting aluminium typically limits the magnetic field range in transport experiments to below 1.5 T in a parallel field and tens of mT in a perpendicular field, where the behavior of the compared materials is almost identical.

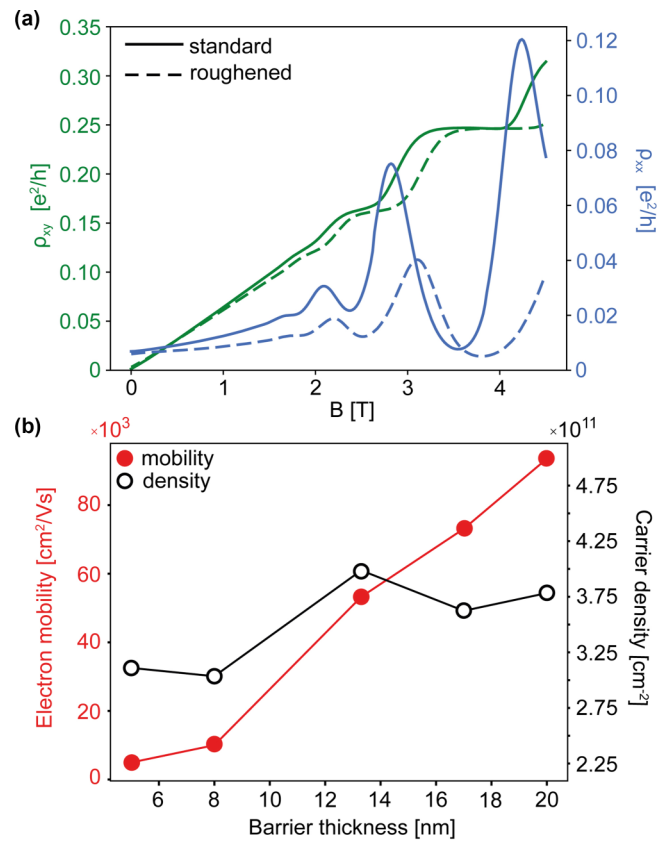


FIG. 6. (a) Hall resistance (green) and longitudinal resistance (blue) as a function of magnetic field for the InAs 2DEG on standard (full line) and intentionally roughened (dashed line) SE surface, after removal of the epitaxial Al. (b) Electron mobility and carrier density as a function of top barrier thickness (for standard structures 2 MLs of GaAs cap and after Al wet etching).

To further investigate the effect of the near-surface structure on the electron mobility, we grew a series of standard samples (capped with 2 MLs of GaAs) with the $\text{In}_{0.75}\text{Ga}_{0.25}\text{As}$ top barrier thickness varying from 5–20 nm. The electron mobility increased almost linearly from 5000 up to 100000 $\text{cm}^2/(\text{V} \cdot \text{s})$ while the density remained between 3×10^{11} and $4 \times 10^{11} \text{ cm}^{-2}$, as shown in Fig. 6(b). This demonstrates that the effect of the intentional roughening of the surface on the electron mobility is indeed negligible in comparison to the effect of other growth parameters and changes in the structural design. An enhancement in mobility is desirable, but an increase in the top barrier thickness can also affect the strength of the proximitized superconductivity, as will be discussed below and in the Supplemental Material [36].

Finally, to assess the influence of the intentional roughening of the SE/SC interface on the superconducting properties of the proximitized system, we investigated the basic characteristics of a top-gated SC-normal-SC (SNS) planar Josephson junction (JJ) device, shown in Fig. 7(a). The JJ device was defined by selectively etching Al (blue) to expose the III-V semiconductor below, which was controlled via an electrostatic gate (gold). The differential resistance $R = V_{AC}/I_{AC}$ as a function of bias current I_{SD} and top-gate voltage V_G , is shown in Fig. 7(b). The transition from superconducting to

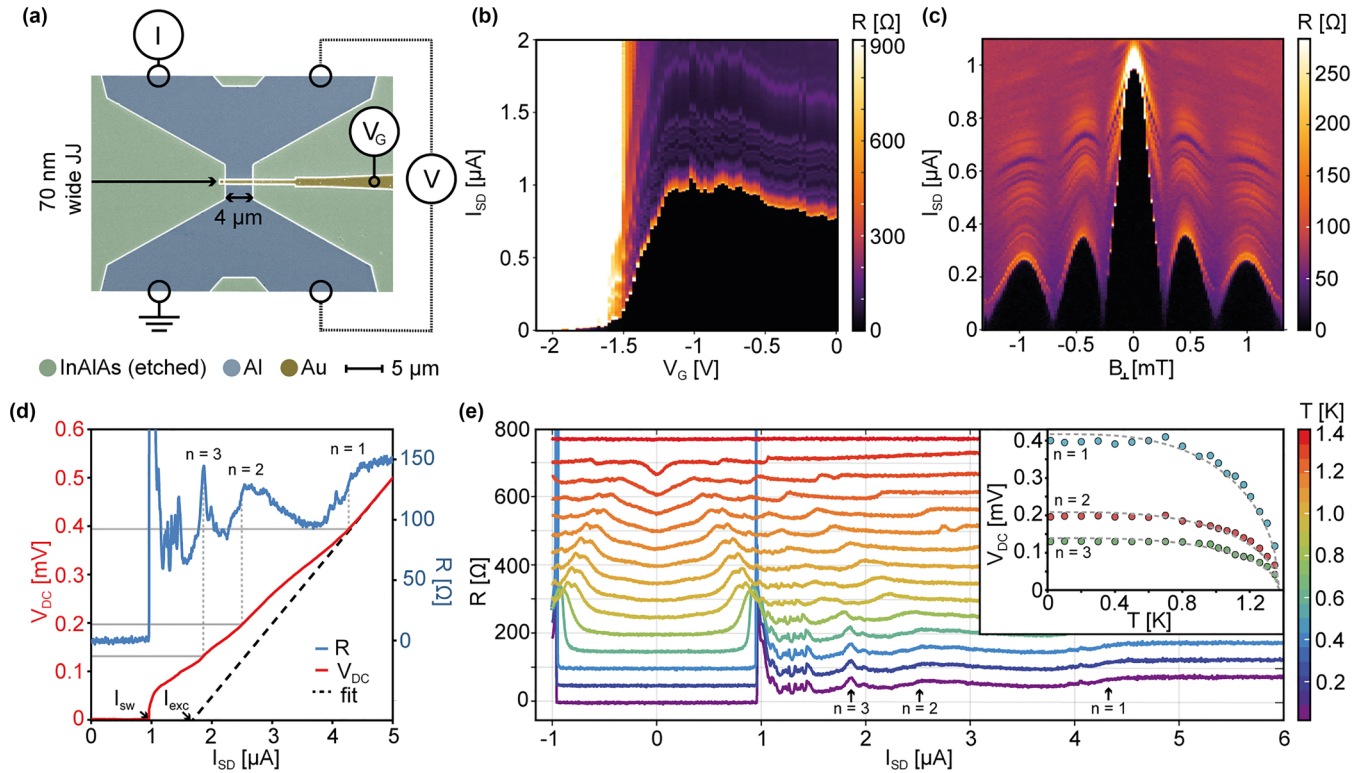


FIG. 7. (a) False-colored SEM image of the measured Josephson junction, highlighting the top-gate (gold) and the epitaxial Al leads of the JJ (blue). The terminals for the bias current $I = I_{SD} + I_{AC}$, measured four-probe voltage V_{DC} and V_{AC} and gate voltage V_G are highlighted. (b) Differential resistance $R = V_{AC}/I_{AC}$ of the JJ as a function of source-drain current I_{SD} and gate voltage V_G . (c) Dependence of R of the JJ as a function of I_{SD} and out-of-plane magnetic field B_{\perp} . (d) Dependence of V_{DC} (red, left axis) and differential resistance R (blue, right axis) on I_{SD} , measured at a base temperature of 18 mK. The black dashed line shows a linear fit to the I-V trace above ~ 0.4 mV. The individual MAR peaks in R are labeled by n . They are related to the measured voltage via the I-V trace (gray dotted lines). The black arrows point to the position of the switching and excess current, respectively. (e) Temperature dependence of R as function of bias current I_{SD} . For clarity, each temperature trace is offset by 50Ω . Extracted V_{DC} positions of the MAR peaks in R for $n = 1, 2, 3$ as a function of temperature are shown in the inset. The dashed lines correspond to fits to the BCS theory for the nominal Al superconducting gap.

the resistive state (at the switching current I_{sw}) was tuned by sweeping V_G , where full suppression of the supercurrent appeared around $V_G = -1.8$ V. For all following experiments we set $V_G = -1.1$ V where we expected the SE segment to be tuned to the single sub-band regime.

Next, we investigated the SC-to-normal transition as a function of the out-of-plane magnetic field B_{\perp} . We observed a Fraunhofer pattern typical for planar JJs, shown in Fig. 7(c). The suppression of the switching current occurs when the flux penetrating the junction area equals the magnetic flux quantum, as further discussed in the Supplemental Material [36]. For large current bias the junction resistance attained a normal state value $R_n = 150 \Omega$ (the same as above the critical temperature of $T_c \approx 1.38$ K).

At zero magnetic field we found a maximum switching current $I_{sw} \approx 1 \mu\text{A}$, and excess current $I_{exc} \approx 1.7 \mu\text{A}$, as shown in Fig. 7(d). Both the products $I_{sw}R_n$ and $I_{exc}R_n$ can be related to the interface transparency and the induced superconducting gap energy [44,45]. This is consistent with other reports in literature and discussed in more detail in the Supplemental Material [36].

The induced gap energy can also be extracted by analyzing the modulation of the differential resistance in the resistive state. This originates from multiple Andreev reflection (MAR)

and became apparent when the current bias was larger than the switching current for both the gate and magnetic field dependencies. The MAR is a signature of coherent charge transport at finite bias within the induced superconducting gap, Δ^* , i.e., at subgap voltages $V_{DC} < 2 \cdot \Delta_{Al}/e$ ($\Delta_{Al} = 1.76 \cdot k_B \cdot T_c \approx 210 \mu\text{eV}$) [44,45]. The position in V_{DC} of individual MAR peaks is related to the size of the induced gap, as shown in Figs. 7(d)–7(e). The induced gap Δ^* is given via $e \cdot V_{DC} = 2 \cdot \Delta^*/n$, where $n = 1, 2, 3, \dots$. This is highlighted in Fig. 7(d) for a measurement at 18 mK. By averaging the value extracted for $n = 1, 2, 3$, we found $\Delta^* = 197 \pm 2 \mu\text{eV}$, which is close to the nominal Δ_{Al} . This value of Δ^* remains almost constant up to 700 mK, as apparent from the dependency of V_{DC} assigned to different n on temperature shown in Fig. 7(e). Above 700 mK, Δ^* starts to change and follows the BCS relation [46] for the Al gap energy $\Delta_{Al}(T, n) = 2/n \cdot \Delta_{Al}(0) \cdot \tanh(1.74\sqrt{T/T_c - 1})$.

To demonstrate the quality of the intentionally roughened material, we compared the measurements to a nominally identical JJ device fabricated from the standard nonroughened material (2 MLs of GaAs). The same analysis of MAR as introduced above yields $\Delta^*_r = 197 \pm 1 \mu\text{eV}$ for the roughened material and $\Delta^*_s = 184 \pm 6 \mu\text{eV}$ for the standard material, both at 500 mK. The similar values of Δ^* together with

the no apparent change in electron mobility, show that the quality of the hybrid material is not significantly affected by the implemented roughening.

Furthermore, we investigated a JJ fabricated from the standard material where the top barrier thickness was increased from 13.4 nm to 20 nm (20 nm top barrier thickness and 2ML GaAs cap). In this case, we observed a reduced number of clear MAR features, which complicated the correct assignment of n , as shown in the Supplemental Material [36]. The analysis yields an upper bound of $\Delta^*_{20\text{nm}} = 170 \mu\text{eV}$ for $n = 2$ at 550 mK, which is lower but still comparable to the samples with a thinner barrier and unexpected in comparison to theoretical predictions [6]. The possibility to increase the electron mobility (i.e., tune the top barrier thickness), while preserving the induced gap size can be advantageous in future device designs. More importantly, it was recently suggested by Awoga *et al.* [47], that a weaker coupling between the SE and SC can mitigate influence of local disorder, which is expected to be one of the significant factors that can impair device performance. A more detailed analysis of the MAR data for all the investigated samples is given in the Supplemental Material [36]. Our results show that more experimental investigations of growth series with consistent change of parameters are necessary to relate the material properties to current theoretical description of hybrid devices.

Overall, we found that all three material designs exhibited a highly transparent interface, gap size comparable to the BCS theory and other reports in literature, signatures of coherent ballistic transport through a JJ and a good performance in our other experiments focused on InAs/Al hybrids [33–35]. In addition, studying differently designed material structures implemented into hybrid devices is important for further understanding of the influence of individual material parameters on transport properties.

VI. CONCLUSION

We have shown how a growth approach based on roughening of the interface between lattice mismatched materials

can be utilized to form defect-free heterostructures. This is demonstrated by improving the crystalline quality of Al thin films within an established SE/SC hybrid material platform. We show that the deposition of 5 MLs of GaAs on the top barrier of a high-quality shallow InAs 2DEG anisotropically roughens the surface. Subsequent *in situ* deposition of a thin epitaxial Al film resulted in the formation of an Al layer with a single-crystal orientation, which remained free of grain boundaries on at least a 5 μm scale.

We found that the introduced roughening did not impair the electron mobility and carrier density of the shallow 2DEG. In addition, the material showed qualities comparable to state-of-the-art SE/SC hybrid JJ-based devices in transport experiments. This implies that local nanotexturing of the semiconductor surface (likely at scales below the Fermi wavelength) does not negatively impact the transport properties of the proximitized system. These results provide an experimental clue to answering a pressing question: What is the role of the detailed crystallography of the SC for the performance of SE/SC hybrid devices? This is still a subject of an extensive debate [23–25,32].

Data supporting this study can be found on Zenodo [48].

ACKNOWLEDGMENTS

We thank Christian Reichl, Stefan Fält, and Mattias Beck for technical support. We also thank Sjoerd Telkamp, Clemens Todt, and Tilman Tröster for fruitful discussions. We thank the IBM Quantum Academic Network for financial support. We acknowledge the support of the Cleanroom Operations Team of the Binnig and Rohrer Nanotechnology Center (BRNC). This work was supported by the Swiss National Center of Competence in Research Quantum Science and Technology, QSIT, together with the European Union and the state of Berlin within the frame of the European Regional Development Fund (ERDF) under Project No. 2016011843 and by Czech Science Foundation Grant No. 22-22000M. F.N. acknowledges support from the European Research Council Grant No. 804273 and the Swiss National Science Foundation Grant No. 200021_201082.

-
- [1] M. Hays, V. Fatemi, D. Bouman, J. Cerrillo, S. Diamond, K. Serniak, T. Connolly, P. Krogstrup, J. Nygård, A. Levy Yeyati *et al.*, *Science* **373**, 430 (2021).
 - [2] T. W. Larsen, K. D. Petersson, F. Kuemmeth, T. S. Jespersen, P. Krogstrup, J. Nygård, and C. M. Marcus, *Phys. Rev. Lett.* **115**, 127001 (2015).
 - [3] L. Casparis, M. R. Connolly, M. Kjaergaard, N. J. Pearson, A. Kringhøj, T. W. Larsen, F. Kuemmeth, T. Wang, C. Thomas, S. Gronin *et al.*, *Nature Nanotechnol.* **13**, 915 (2018).
 - [4] S. Das Sarma, M. Freedman, and C. Nayak, *npj Quantum Inf.* **1**, 15001 (2015).
 - [5] P. Krogstrup, N. Ziino, W. Chang, S. Albrecht, M. Madsen, E. Johnson, J. Nygård, C. M. Marcus, and T. Jespersen, *Nature Mater.* **14**, 400 (2015).
 - [6] J. Shabani, M. Kjaergaard, H. J. Suominen, Y. Kim, F. Nichele, K. Pakrouski, T. Stankevici, R. M. Lutchyn, P. Krogstrup, R. Feidenhans'l, S. Kraemer, C. Nayak, M. Troyer, C. M. Marcus, and C. J. Palmstrøm, *Phys. Rev. B* **93**, 155402 (2016).
 - [7] A. E. G. Mikkelsen, P. Kotetes, P. Krogstrup, and K. Flensberg, *Phys. Rev. X* **8**, 031040 (2018).
 - [8] W. Chang, S. Albrecht, T. Jespersen, F. Kuemmeth, P. Krogstrup, J. Nygård, and C. M. Marcus, *Nature Nanotechnol.* **10**, 232 (2015).
 - [9] V. Mourik, K. Zuo, S. M. Frolov, S. Plissard, E. P. Bakkers, and L. P. Kouwenhoven, *Science* **336**, 1003 (2012).
 - [10] S. Vaitiekėnas, G. Winkler, B. van Heck, T. Karzig, M.-T. Deng, K. Flensberg, L. Glazman, C. Nayak, P. Krogstrup, R. Lutchyn *et al.*, *Science* **367**, eaav3392 (2020).
 - [11] O. Kürtössy, Z. Scherübl, G. Fülöp, I. E. Lukács, T. Kanne, J. Nygård, P. Makk, and S. Csonka, *Nano Lett.* **21**, 7929 (2021).
 - [12] C. Reeg, D. Loss, and J. Klinovaja, *Beilstein J. Nanotechnol.* **9**, 1263 (2018).

- [13] M. Aghaee, A. Akkala, Z. Alam, R. Ali, A. A. Ramirez, M. Andrzejczuk, A. E. Antipov, M. Astafev, B. Bauer, J. Becker *et al.*, *Phys. Rev. B* **107**, 245423 (2023).
- [14] W. L. Sarney, S. P. Svensson, K. S. Wickramasinghe, J. Yuan, and J. Shabani, *J. Vacuum Sci. Technol. B* **36**, 062903 (2018).
- [15] W. L. Sarney, S. P. Svensson, A. C. Leff, W. F. Schiela, J. O. Yuan, M. C. Dartiailh, W. Mayer, K. S. Wickramasinghe, and J. Shabani, *J. Vacuum Sci. Technol. B* **38**, 032212 (2020).
- [16] T. Wang, C. Thomas, R. E. Diaz, S. Gronin, D. Passarello, G. C. Gardner, M. A. Capano, and M. J. Manfra, *J. Cryst. Growth* **535**, 125570 (2020).
- [17] U. S. Pracht, N. Bachar, L. Benfatto, G. Deutscher, E. Farber, M. Dressel, and M. Scheffler, *Phys. Rev. B* **93**, 100503(R) (2016).
- [18] N. Court, A. Ferguson, and R. Clark, *Supercond. Sci. Technol.* **21**, 015013 (2008).
- [19] L. Nguyen, T. Hashimoto, D. N. Zakharov, E. A. Stach, A. P. Rooney, B. Berkels, G. E. Thompson, S. J. Haigh, and T. L. Burnett, *ACS Appl. Mater. Interfaces* **10**, 2230 (2018).
- [20] M. Kjaergaard, F. Nichele, H. J. Suominen, M. P. Nowak, M. Wimmer, A. R. Akhmerov, J. A. Folk, K. Flensberg, J. Shabani, C. J. Palmstrøm *et al.*, *Nature Commun.* **7**, 1 (2016).
- [21] C. J. Richardson, N. P. Siwak, J. Hackley, Z. K. Keane, J. E. Robinson, B. Arey, I. Arslan, and B. S. Palmer, *Supercond. Sci. Technol.* **29**, 064003 (2016).
- [22] N. P. de Leon, K. M. Itoh, D. Kim, K. K. Mehta, T. E. Northup, H. Paik, B. Palmer, N. Samarth, S. Sangtawesin, and D. Steuerman, *Science* **372**, eabb2823 (2021).
- [23] W. S. Cole, J. D. Sau, and S. Das Sarma, *Phys. Rev. B* **94**, 140505(R) (2016).
- [24] C. Reeg, D. Loss, and J. Klinovaja, *Phys. Rev. B* **97**, 165425 (2018).
- [25] S. N. Thomas, S. Das Sarma, and J. D. Sau, *Phys. Rev. B* **106**, 174501 (2022).
- [26] S. A. Khan, S. Martí-Sánchez, D. Olsteins, C. Lampadaris, D. J. Carrad, Y. Liu, J. Quiñones, M. C. Spadaro, T. S. Jespersen, P. Krogstrup *et al.*, *ACS Nano* **17**, 11794 (2023).
- [27] T. Kanne, M. Marnauza, D. Olsteins, D. J. Carrad, J. E. Sestoft, J. de Bruijckere, L. Zeng, E. Johnson, E. Olsson, K. Grove-Rasmussen *et al.*, *Nature Nanotechnol.* **16**, 776 (2021).
- [28] Y. Liu, S. Vaitiekėnas, S. Martí-Sánchez, C. Koch, S. Hart, Z. Cui, T. Kanne, S. A. Khan, R. Tanta, S. Upadhyay *et al.*, *Nano Lett.* **20**, 456 (2020).
- [29] F. Krizek, J. E. Sestoft, P. Aseev, S. Marti-Sanchez, S. Vaitiekėnas, L. Casparis, S. A. Khan, Y. Liu, T. Stankevič, A. M. Whiticar *et al.*, *Phys. Rev. Mater.* **2**, 093401 (2018).
- [30] C. M. Moehle, C. T. Ke, Q. Wang, C. Thomas, D. Xiao, S. Karwal, M. Lodari, V. van de Kerkhof, R. Termaat, G. C. Gardner *et al.*, *Nano Lett.* **21**, 9990 (2021).
- [31] C. Thomas, R. E. Diaz, J. H. Dycus, M. E. Salmon, R. E. Daniel, T. Wang, G. C. Gardner, and M. J. Manfra, *Phys. Rev. Mater.* **3**, 124202 (2019).
- [32] M. Pendharkar, B. Zhang, H. Wu, A. Zarassi, P. Zhang, C. Dempsey, J. Lee, S. Harrington, G. Badawy, S. Gazibegovic *et al.*, *Science* **372**, 508 (2021).
- [33] D. Z. Haxell, E. Cheah, F. Krizek, R. Schott, M. F. Ritter, M. Hinderling, W. Belzig, C. Bruder, W. Wegscheider, H. Riel *et al.*, *Phys. Rev. Lett.* **130**, 087002 (2023).
- [34] D. Z. Haxell, M. Coraiola, D. Sabonis, M. Hinderling, S. ten Kate, E. Cheah, F. Krizek, R. Schott, W. Wegscheider, W. Belzig *et al.*, [arXiv:2212.03554](https://arxiv.org/abs/2212.03554).
- [35] M. Hinderling, D. Sabonis, S. Paredes, D. Z. Haxell, M. Coraiola, S. C. ten Kate, E. Cheah, F. Krizek, R. Schott, W. Wegscheider *et al.*, *Phys. Rev. Appl.* **19**, 054026 (2023).
- [36] See Supplemental Material at <http://link.aps.org/supplemental/10.1103/PhysRevMaterials.7.073403> for following details: Methods, S1: Surface of InAs 2DEGs, S2: Extraction of lattice spacings, S3: Controlled oxidation of Al, S4: *In situ* annealing STEM experiment, S5: Aging of studied lamellae, S6: STEM tomography, S7: Additional analysis of the JJ measurements of the roughened sample, S8: JJ measurements of the standard, nonroughened samples. It contains Refs. [49–63].
- [37] L. Nicolai, K. Biermann, and A. Trampert, *Ultramicroscopy* **224**, 113261 (2021).
- [38] K. Ohta, T. Kojima, and T. Nakagawa, *J. Cryst. Growth* **95**, 71 (1989).
- [39] A. Diéguez, A. Vilà, A. Cornet, S. A. Clark, D. I. Westwood, and J. R. Morante, *J. Vacuum Sci. Technol. B* **15**, 687 (1997).
- [40] Y. Chen, Z. Chen, J. Li, Y. Chen, C. Li, J. Zhan, T. Yu, X. Kang, F. Jiao, S. Li *et al.*, *CrystEngComm* **20**, 6811 (2018).
- [41] X. Feng, T. Yu, Y. Wei, C. Ji, Y. Cheng, H. Zong, K. Wang, Z. Yang, X. Kang, G. Zhang *et al.*, *ACS Appl. Mater. Interfaces* **8**, 18208 (2016).
- [42] S. Pauka, J. Witt, C. Allen, B. Harlech-Jones, A. Jouan, G. Gardner, S. Gronin, T. Wang, C. Thomas, M. Manfra *et al.*, *J. Appl. Phys.* **128**, 114301 (2020).
- [43] A. Hatke, T. Wang, C. Thomas, G. Gardner, and M. Manfra, *Appl. Phys. Lett.* **111**, 142106 (2017).
- [44] K. Flensberg, J. B. Hansen, and M. Octavio, *Phys. Rev. B* **38**, 8707 (1988).
- [45] M. Kjaergaard, H. J. Suominen, M. P. Nowak, A. R. Akhmerov, J. Shabani, C. J. Palmstrøm, F. Nichele, and C. M. Marcus, *Phys. Rev. Appl.* **7**, 034029 (2017).
- [46] J. R. Waldram, *Superconductivity of Metals and Cuprates* (IOP Publishing, Bristol, 1996).
- [47] O. A. Awoga, M. Leijnse, A. M. Black-Schaffer, and J. Cayao, *Phys. Rev. B* **107**, 184519 (2023).
- [48] [10.5281/zenodo.8091280](https://zenodo.org/record/8091280).
- [49] M. Weilmeyer, K. Colbow, T. Tiedje, T. Van Buuren, and L. Xu, *Can. J. Phys.* **69**, 422 (1991).
- [50] P. Klapetek, D. Nečas, A. Campbellová, A. Yacoot, and L. Koenders, *Meas. Sci. Technol.* **22**, 025501 (2011).
- [51] J. Schindelin, I. Arganda-Carreras, E. Frise, V. Kaynig, M. Longair, T. Pietzsch, S. Preibisch, C. Rueden, S. Saalfeld, B. Schmid *et al.*, *Nature Meth.* **9**, 676 (2012).
- [52] K. Momma and F. Izumi, *J. Appl. Crystallogr.* **41**, 653 (2008).
- [53] P. A. Rosenthal, M. R. Beasley, K. Char, M. S. Colclough, and G. Zaharchuk, *Appl. Phys. Lett.* **59**, 3482 (1991).
- [54] H. J. Suominen, J. Danon, M. Kjaergaard, K. Flensberg, J. Shabani, C. J. Palmstrøm, F. Nichele, and C. M. Marcus, *Phys. Rev. B* **95**, 035307 (2017).
- [55] M. C. Dartiailh, J. J. Cuzzo, B. H. Elfeky, W. Mayer, J. Yuan, K. S. Wickramasinghe, E. Rossi, and J. Shabani, *Nature Commun.* **12**, 78 (2021).
- [56] K. Likharev, *Rev. Mod. Phys.* **51**, 101 (1979).
- [57] B. K. Nikolić, J. K. Freericks, and P. Miller, *Phys. Rev. B* **64**, 212507 (2001).

- [58] Y. G. Naidyuk and K. Gloos, *Low Temp. Phys.* **44**, 257 (2018).
- [59] S. N. Artemenko, A. Volkov, and A. Zaitsev, *Solid State Commun.* **30**, 771 (1979).
- [60] J. S. Lee, B. Shojaei, M. Pendharkar, A. P. McFadden, Y. Kim, H. J. Suominen, M. Kjaergaard, F. Nichele, H. Zhang, C. M. Marcus *et al.*, *Nano Lett.* **19**, 3083 (2019).
- [61] A. Chrestin, T. Matsuyama, and U. Merkt, *Phys. Rev. B* **55**, 8457 (1997).
- [62] B. A. Aminov, A. A. Golubov, and M. Y. Kupriyanov, *Phys. Rev. B* **53**, 365 (1996).
- [63] T. Schäpers, *Superconductor/Semiconductor Junctions* (Springer, Berlin, 2001), Vol. 174.